Supplementary Figure 1

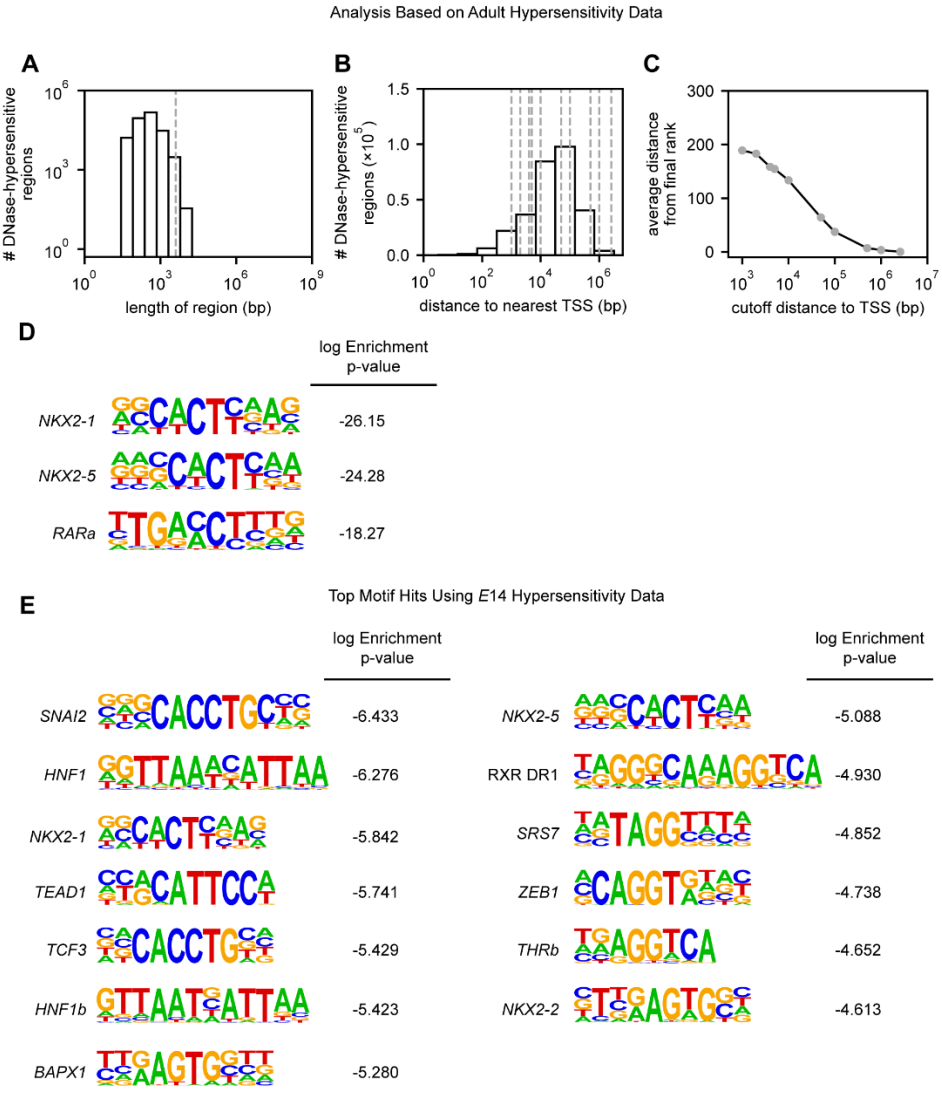

Fig. S1. Transcription-factor-binding motifs identified using a novel bioinformatics approach. **A)** Histogram of the lengths of all investigated DNase-hypersensitive regions from adult mouse lung ENCODE data. Dashed line shows the maximum length of a DNase-hypersensitive region that was included. **B)** Histogram of the distance of each DNase-hypersensitive region to the nearest TSS in the genome, using adult lung data. **C)** All identified TF motifs were ranked by their enrichment *p*-values in DNase-hypersensitive regions within different distances of the TSS in our dataset (corresponding to dashed lines in B). Datapoints represent the average difference in rank between TFs at each cutoff distance and their rank at the largest cutoff distance. **D)** Top three identified motifs using adult lung DNase-hypersensitivity data. **E)** Top 13 motifs identified using *E*14 lung DNase-hypersensitivity data. TSS, transcription start site; bp, base pairs; TF, transcription factor.

Supplementary Figure 2

A high ΔP

gene	log_2(fold change)	adjusted *p*
Rbp4	0.543	0.431
Stra6	-0.173	0.834
Rdh1	0.590	0.524
Rdh9	1.400	0.0789
Rdh10	-0.658	0.159
Rdh11	0.026	0.928
Rdh12	-0.244	0.672
Rdh13	-0.120	0.744
Dhrs3	-0.316	0.223
Hsd17b11	0.226	0.571
Bcmo1	0.195	0.855
Lrat	0.333	0.679
Aldh1a2 (Raldh2)	-0.361	0.492
Aldh1a3 (Raldh3)	-0.592	0.258
Cyp26a1	-0.721	0.376
Crabp2	-0.088	0.859
Nr2f2	0.105	0.784
Rara	-0.285	0.321
Rarb	-0.328	0.119
Rarg	0.019	0.981
Rxra	0.480	0.111
Rxrb	0.231	0.654
Rxrg	-0.907	0.0997

B epithelial *Yap* KO

gene	log_2(fold change)	adjusted *p*
Rbp2	-2.303	1
Rdh9	-0.468	1
Rdh11	0.152	0.228
Rdh12	0.373	0.284
Rdh13	0.011	0.93
Rdh14	0.143	0.368
Adh4	0.435	1
Hsd17b11	0.230	0.121
Hsd17b13	-0.960	1
Bcmo1	-1.066	1
Aldh1a2 (Raldh2)	0.006	0.957
Aldh1a3 (Raldh3)	-0.636	1
Aldh8a1	-1.002	1
Cyp26a1	1.240	1
Cyp26b1	-0.069	0.635
Cyp26c1	0.304	1
Rara	-0.032	0.779
Rarb	-0.077	0.524
Rxra	-0.062	0.548
Rxrb	-0.096	0.377
Rxrg	0.007	0.98

Fig. S2. Relative expression and adjusted *p* value of genes in the RA biosynthetic pathway that are differentially expressed **A)** under high ΔP or **B)** when *Yap* is deleted from the epithelium. See Figure 2C,E for significantly diferent pathway components and Figure 2D,F for volcano plots of these genes.

Supplementary Figure 3

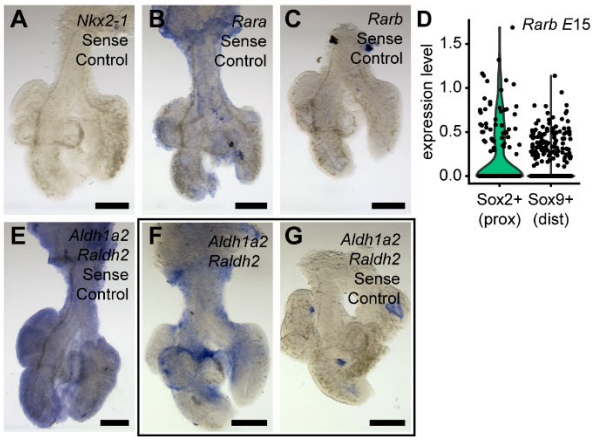

Fig. S3. Negative controls for *in situ* hybridization. Lungs incubated with positive sense (negative control) *in situ* hybridization probes for **A)** *Nkx2-1*, **B)** *Rara*, **C)** *Rarb*, and **E)** *Aldh1a2* developed in parallel with the explants shown in **Figure 3**. Lungs incubated with **F)** antisense and **G)** sense *in situ* hybridization probes for *Aldh1a2* for a shorter development time show a similar pattern of staining as in Figure 3H and very little sense staining compared to panel E. All scale bars, 250 μm. **D)** *Rarb* expression in scRNA-seq data from *E*15.5 airway epithelial cells. *Sox2* is expressed in the proximal (prox) airway epithelium and *Sox9* is expressed in the distal (dist) airway epithelium.

Supplementary Figure 4

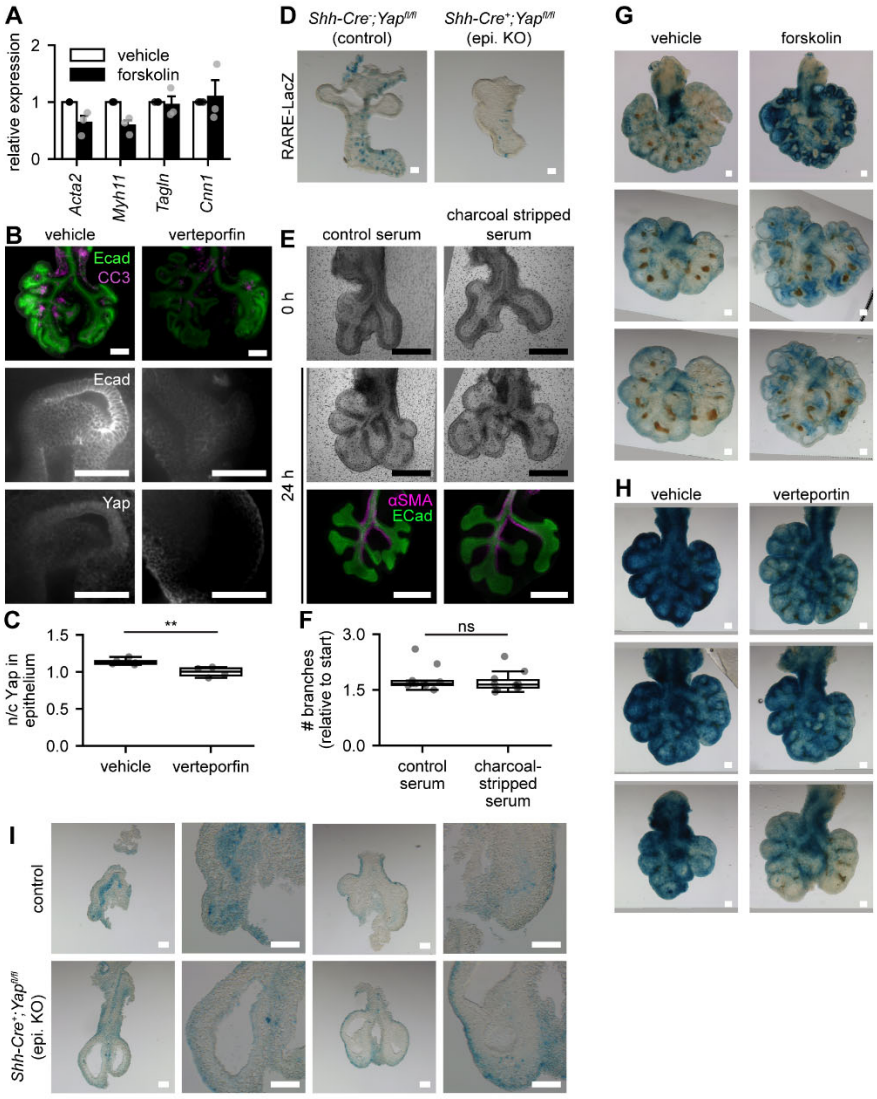

Fig. S4. Effects of forskolin, verteporfin, and *Yap* knockout on *E*11.5 lung explants. **A**) X-gal staining in *E*11.5 lungs explanted from *RARE-LacZ* reporter mice cultured in the presence of forskolin or vehicle control (DMSO) for 48 h. **B)** qRT-PCR analysis for smooth muscle gene markers in lungs cultured in the presence of forskolin or DMSO for 48 h. Shown are mean + s.e.m. Datapoints represent pooled RNA from 2-3 lungs from 3 independent experiments. **C)** Immunofluorescence analysis for Ecad, cleaved caspase 3 (CC3), and Yap in *E*11.5 lung explants cultured in the presence of verteporfin or vehicle control for 24 h. Scale bars: top row, 100 μm; bottom two rows, 50 μm. **D)** Quantification of the ratio of nuclear to cytoplasmic Yap staining in *E*11.5 lung explants cultured in the presence of verteporfin or vehicle control for 24 h. $p = 0.00700$ as denoted by Student's t-test. **E)** X-gal staining in *E*11.5 lungs explanted from *RARE-LacZ* reporter mice cultured in the presence of verteporfin or vehicle control (DMSO) for 48 h. X-gal staining in *E*11.5 *Shh-Cre;Yap$^{fl/fl}$;RARE-LacZ* epithelial *Yap* knockout (epi. KO) reporter **F**) lungs or **G**) mesenchyme-free epithelium. A, E, scale bars, 100 μm.

Supplementary Figure 5

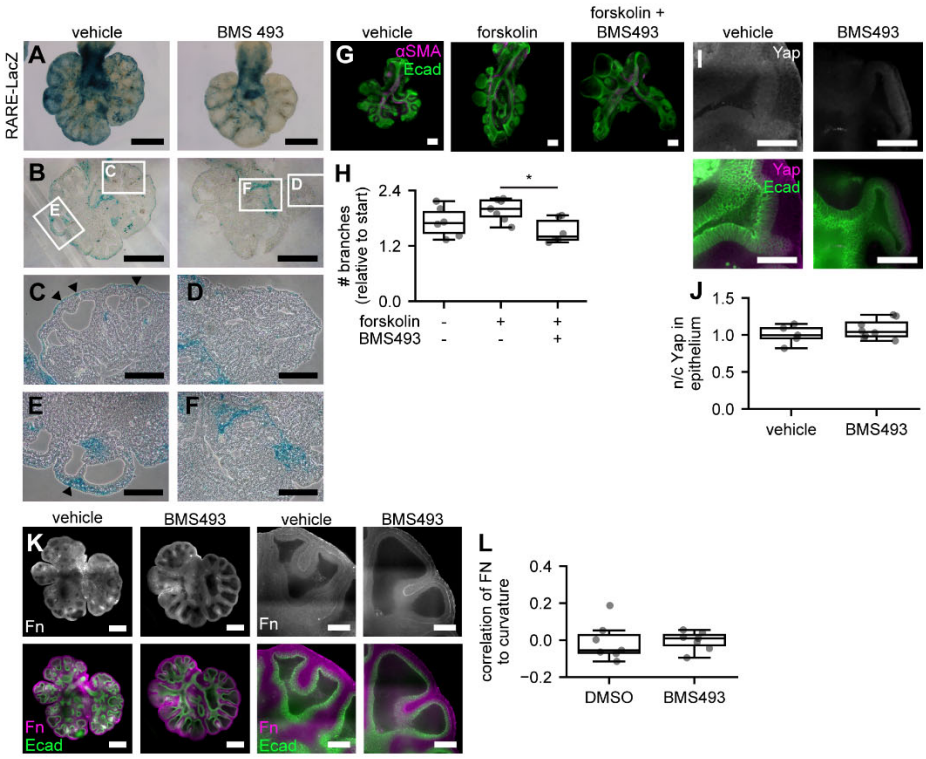

Fig. S5. Inhibiting RA signaling by treating RARE-LacZ reporter mouse lung explants with BMS493 decreases X-gal staining. **A)** Lungs cultured for 24 h in media supplemented with charcoal-stripped serum or non-charcoal stripped serum (control serum); brightfield scale bars, 500 μm; immunofluorescence scale bars, 250 μm. **B)** Relative change in the number of branches in *E*11.5 lung explants cultured in control medium or in medium containing charcoal-stripped serum for 24 h. X-gal stains of **C)** whole mounts and **D-H)** sections of lungs explanted from *RARE-LacZ* reporter mice cultured in the presence of BMS493 or vehicle control (DMSO) for 48 h. Scale bars: A, B 500 μm; C-F, 200 μm. Arrowheads indicate regions of darker X-gal stain in the mesothelium of controls. **I)** Immunofluorescence analysis for Yap and Ecad (scale bars, 50 μm) and **J)** quantification of the ratio of nuclear to cytoplasmic Yap in the epithelium in *E*11.5 lung explants cultured in the presence of BMS493 or vehicle control for 48 h. **K)** Immunofluorescence analysis for Ecad and αSMA and **L)** quantification of the number of epithelial branches in *E*11.5 lung explants cultured in the presence of forskolin, forskolin and BMS493, or vehicle control for 24 h. $p = 0.0250$ as denoted by one-way ANOVA, $p = 0.0201$ as denoted by Tukey's post-hoc test between lungs cultured in the presence of forskolin and lungs cultured in the presence of forskolin and BMS493. Scale bars, 100 μm.
M) Immunofluorescence analysis for fibronectin and Ecad (scale bars, left 200 μm; right 50 μm), and **N)** quantification of the correlation of fibronectin staining intensity to epithelial curvature in *E*11.5 lung explants cultured in the presence of BMS493 or vehicle control for 48 h.

Supplementary Figure 6

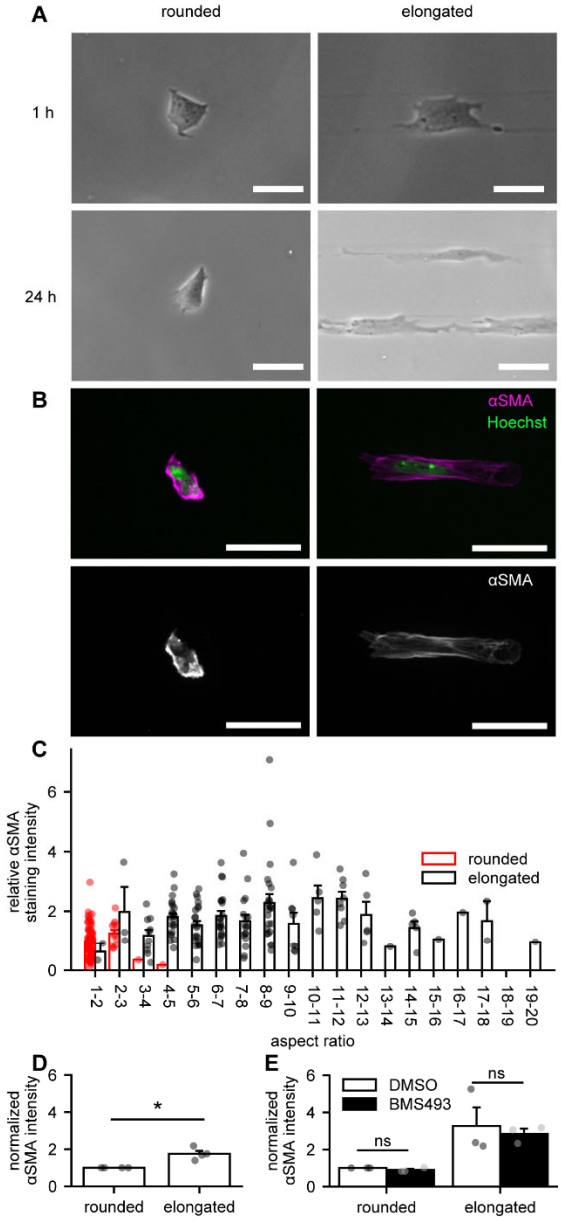

Fig. S6. Inhibiting RA signaling does not directly affect the differentiation of primary embryonic lung mesenchyme into smooth muscle cells. **A)** Phase-contrast images of cells on squares (rounded cells) or lines (elongated cells) of fibronectin after 1 h or 24 h of culture; scale bars, 50 µm. **B)** Immunofluorescence analysis for αSMA in rounded or elongated cells after 24 h of culture. Scale bars, 50 µm. **C)** Quantification of αSMA staining intensity in cells of different aspect ratios in panel B. Datapoints represent individual cells from 4 independent experiments. **D)** Quantification of average αSMA staining intensity in elongated versus rounded cells in panel B. Datapoints represent averages of all cells from each of 4 independent experiments. $p = 0.0189$ as denoted by Student's t-test. **E)** Quantification of αSMA staining intensity in rounded or elongated cells cultured with or without BMS493. Datapoints represent averages of all cells from each of 3 independent experiments. Shown are mean + s.e.m. ns, not significant.

Supplementary Figure 7

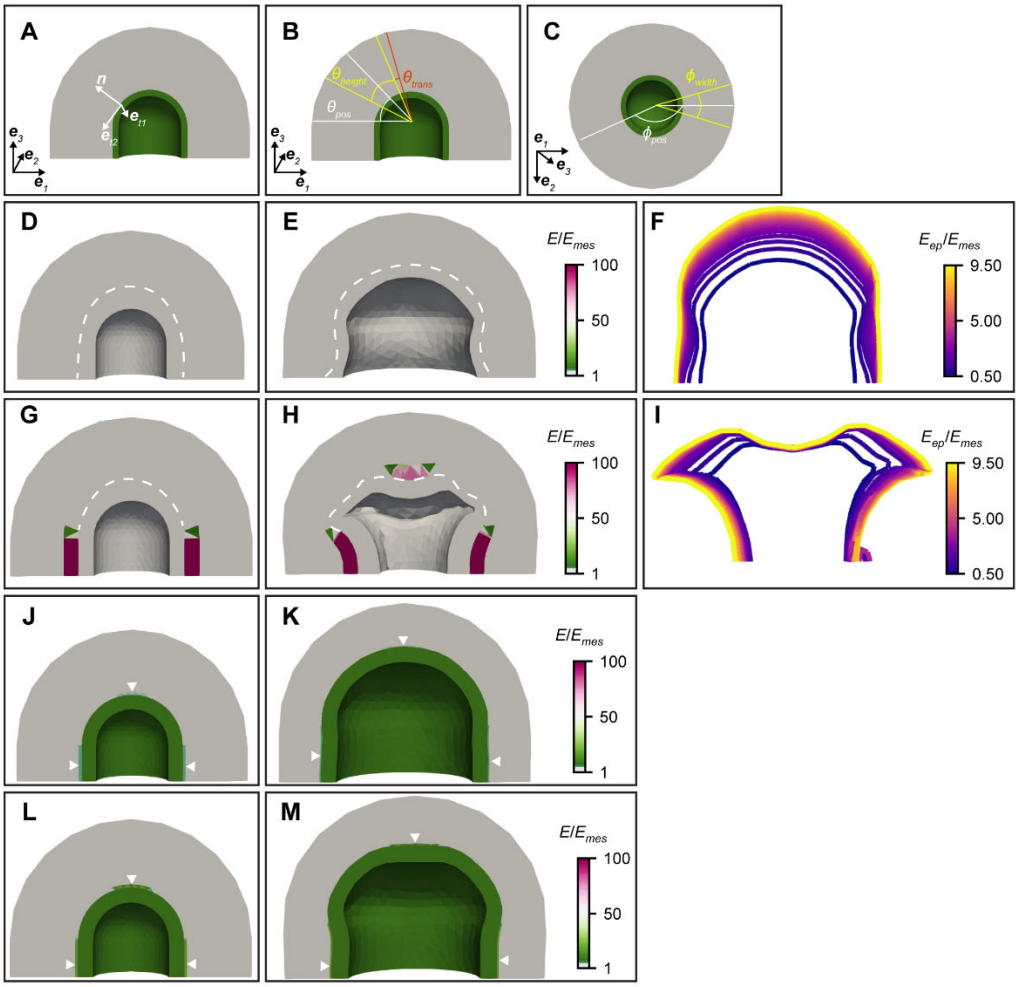

Fig. S7. Geometric parameters of the computational model. **A)** Epithelial coordinate system consisting of the normal vector and two tangent vectors to the epithelium. **B)** Angles in the $\boldsymbol{e_1}$-$\boldsymbol{e_3}$ plane between which epithelial proliferation is increased in models with increased proliferation along the flanks of the epithelium. **C)** Angles in the $\boldsymbol{e_1}$-$\boldsymbol{e_2}$ plane between which epithelial proliferation is increased in models with increased proliferation along the flanks of the epithelium. Initial geometries of simulations with $E_{ep} = E_{mes}$ and **D)** no ASM, or **G)** ASM. Initial geometries of simulations without ASM but with a thin layer of mesenchyme of stiffness **J)** $0.3E_{ep}$ or **L)** $2E_{ep}$ adjacent to the mesenchyme in a similar spatial pattern to the ASM of other models. **E, H, K, M)** Final geometries of simulations in panels D, G, J, and L respectively. Arrowheads in J, K, L, and M point to areas of increased mesenchymal stiffness. **F, I)** Final geometries of simulations using different epithelial stiffnesses for the classes of models represented by panels D and G, respectively.

Supplementary Figure 8

A

gene	log_2(fold change)	adjusted *p*	role in ASM differentiation
Shh	-2.757	5.00×10^{-5}	▲
Fgf9	0.201	0.279	▼
BMP4	0.583	5.00×10^{-5}	▲
Tgfb1	0.009	0.953	▲
Tgfb2	-0.911	5.00×10^{-5}	▲
Tgfb3	-1.122	5.00×10^{-5}	▲
Acta2	-1.064	5.00×10^{-5}	ASM marker
Actg2	-2.379	5.00×10^{-5}	ASM marker
Myh11	-2.175	5.00×10^{-5}	ASM marker
Tagln	-1.061	4.65×10^{-3}	ASM marker
Cnn1	-0.331	0.548	ASM marker
Cald1	-0.319	3.20×10^{-3}	ASM marker
Actn1	-0.196	0.0597	ASM marker
Actn2	3.371	5.00×10^{-5}	ASM marker
Actn3	0.945	4.05×10^{-3}	ASM marker
Actn4	-0.265	0.0104	ASM marker
Speg	0.382	0.0154	ASM marker
Lpp	0.263	0.0853	ASM marker
Srf	-0.057	0.851	ASM marker
Myocd	-1.279	5.00×10^{-5}	ASM marker
Mkl1	-0.115	0.384	ASM marker
Mkl2	0.431	5.00×10^{-5}	ASM marker
Lmod1	-2.214	5.00×10^{-5}	ASM marker
Des	1.103	5.00×10^{-5}	ASM marker
Vim	0.059	0.586	ASM marker
Vcl	-0.106	0.442	ASM marker
Mylk	-0.464	5.00×10^{-5}	ASM marker
Smtn	-0.354	1.45×10^{-3}	ASM marker
Heyl	-0.558	1.50×10^{-4}	ASM marker
Nog	-0.829	1.50×10^{-4}	ASM marker
Cspg4	0.080	0.592	ASM marker
Foxf1	-1.005	5.00×10^{-5}	ASM marker
Gata5	0.454	5.00×10^{-5}	ASM marker

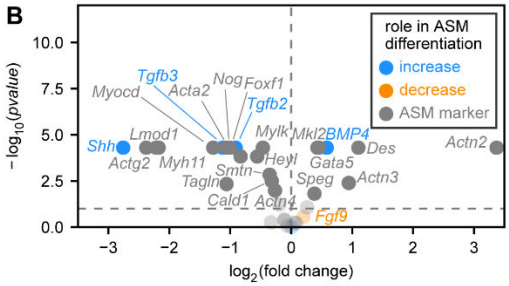

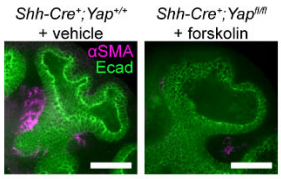

Fig. S8. Expression of ASM genes is modulated by Yap and ΔP. **A)** Relative expression, adjusted *p* value, and expected effect on ASM differentiation or marker status of ASM-controlling or marker genes that are significantly differentially expressed in the lung when *Yap* is conditionally knocked out in the airway epithelium. **B)** Volcano plot of the gene expression changes from A. **C)** Immunofluorescence analysis for αSMA and Ecad in *E*11.5 *Shh-Cre;Yap*$^{fl/fl}$ or littermate control lungs cultured in the presence of forskolin or vehicle control for 48 h. Scale bars, 50 µm.

Supplementary Figure 9

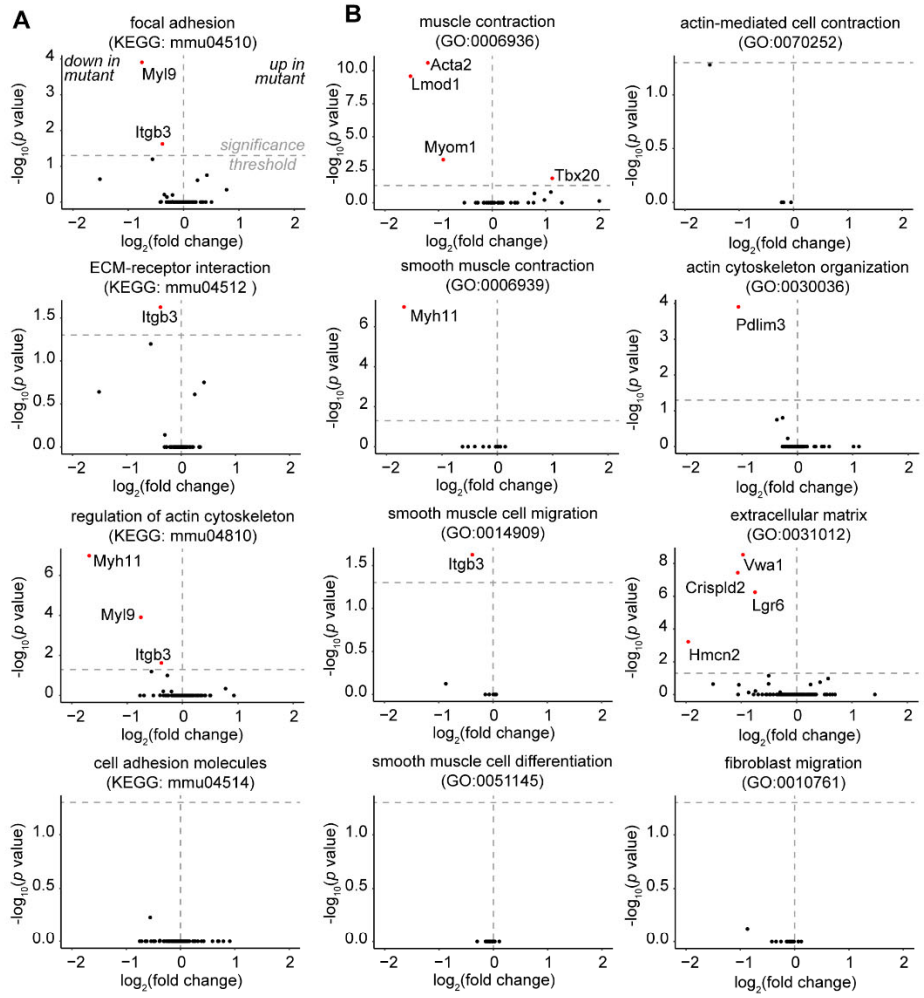

Fig. S9. *Myocd* knockout has a small effect on expression of genes involved in smooth muscle differentiation, ECM adhesion, and cytoskeletal organization. Volcano plots of relative expression and adjusted *p* value of genes involved in ECM deposition and adhesion and smooth muscle differentiation, cytoskeletal organization, and contraction from *E*13.5 lungs with mesenchymal *Myocd* knockout organized by the relevant **A)** Kyoto Encyclopedia of Genes and Genomes (KEGG) pathways and **B)** gene ontology (GO) groupings.

Table S1. Relative changes and *p*-values for differentially expressed genes in explanted *E*12.5 mouse lungs cultured under 200 or 20 Pa ΔP for 48 h, as described in (Nelson et al., 2017) Click here to download Table S1

Table S2. Primers used to genotype transgenic mice and embryos.

Gene	Sequence (5' → 3')	Reference
Yap^{fl}	F: AGGACAGCCAGGACTACACAG R: CACCAGCCTTTAAATTGAGAAC	Jackson Labs
Cre	F: GCATTACCGGTCGATGCAACGAGTGATGAG R: GAGTGAACGAACCTGGTCGAAATCAGTGCG	-
LacZ	F: ATCCTCTGCATGGTCAGGTC R: CGTGGCCTGATTCATTCC	Jackson Labs

Table S3. Primer sequences used for qRT-PCR.

Target	Symbol	Sequence (5' → 3')	Reference
18S ribosomal subunit	18S	F: TCAGATACCGTCGTAGTTC R: CCTTTAAGTTTCAGCTTTGC	(Lee et al., 2012)
α-smooth muscle actin	*Acta2*	F: GCATCCACGAAACCACCTA R: CACGAGTAACAAATCAAAGC	(Sousa et al., 2007)
transgelin	*Tagln*	F: TCCAGTCCACAAACGACCAAGC R: GAATTGAGCCACCTGTTCCATCTG	(Tanaka et al., 2008)
smooth muscle myosin heavy chain	*Myh11*	F: GCTAATCCACCCCCGGAGTA R: TCGCTGAGCTGCCCTTTCT	(Wilczewski et al., 2018)
calponin	*Cnn1*	F: ATGTCTTCTGCACATTTTAACC R: GCTCAAATCTCCGCTCTTG	(Hayashi et al., 2006)
serum response factor	*Srf*	F: GCTTCACCAGATGGCTGTGATA R: AATAAGTGGTGCCGTCCCTTG	(Schlesinger et al., 2011)
retinoic acid receptor-β	*Rarb*	F: TAGAAAACGACGACCCAGCA R: TGGGGTCAAGGGTTCATGTC	(Ng-Blichfeldt et al., 2018)

Table S4. Antibodies used for immunostaining.

Target	Species	Antibody Dilution	Source	Product Number
E-cadherin	Rabbit	1:200	Cell Signaling	24E10
E-cadherin	Rat IgG2a	1:200	ThermoFisher	13-1900
α-smooth muscle actin	Mouse	1:400	Millipore-Sigma	A5228
α-smooth muscle actin	Rabbit	1:200	Abcam	ab5694
Yap1	Rabbit	1:200	Novus Biologicals	NB110-58358
fibronectin	Rabbit	1:200	Sigma-Aldrich	F3648
cleaved caspase-3	Rabbit	1:200	Cell Signaling	9661S
anti-mouse alexa fluor 594	Goat	1:200	ThermoFisher	A11032
anti-mouse alexa fluor 647	Goat	1:200	ThermoFisher	A21235
anti-rabbit alexa fluor 488	Goat	1:200	ThermoFisher	A11034
anti-rabbit alexa fluor 594	Goat	1:200	ThermoFisher	A11012
anti-rabbit alexa fluor 647	Goat	1:200	ThermoFisher	A21245
anti-rat alexa fluor 488	Goat	1:200	ThermoFisher	A11006
anti-rat alexa fluor 594	Goat	1:200	ThermoFisher	A11007

Table S5. Primers used to generate probes for *in situ* hybridization.

Gene	Sequence (5' → 3')	Reference
Rara	F: ATGGGGTCAGCGCCTGTGAGG R: AGCGGCTCTTGCAGCATGTCC	-
Rarb	F: TGGAGTTCGTGGACTTTTCTG R: GCTCCGCTGTCATCTCATA	-
Nkx2-1 (*Ttf1*)	F: CAACAACTGCAGCAGGACAG R: GTCCGACCATAAAGCAAGGTAG	(Visel et al., 2004)
Aldh1a2 (*Raldh2*)	F: TGCTGATGTTCACCTGGAA R: TGCGGAGGATACCATGAG	-

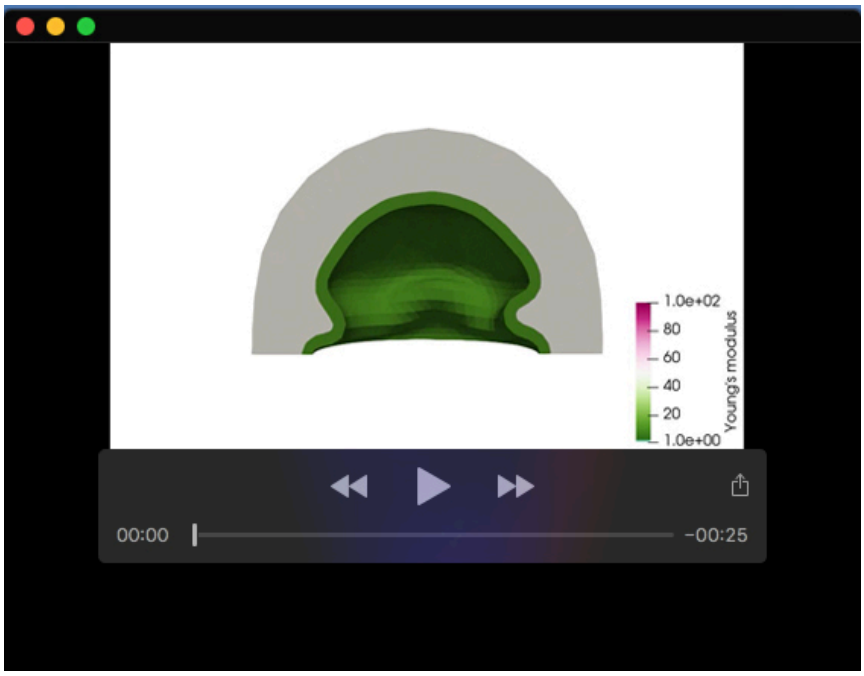

Movie 1. Computational model without smooth muscle. Related to Figure 6D,E.

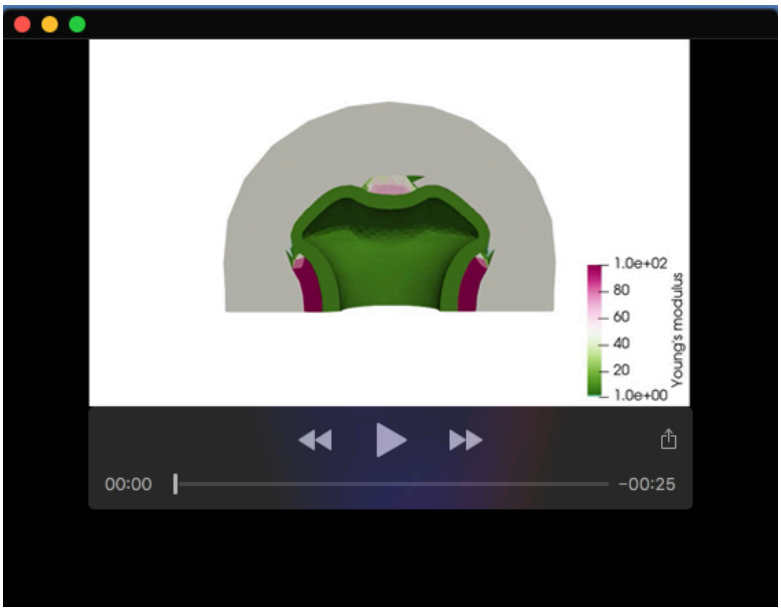

Movie 2. Computational model with smooth muscle. Related to Figure 6G,H.

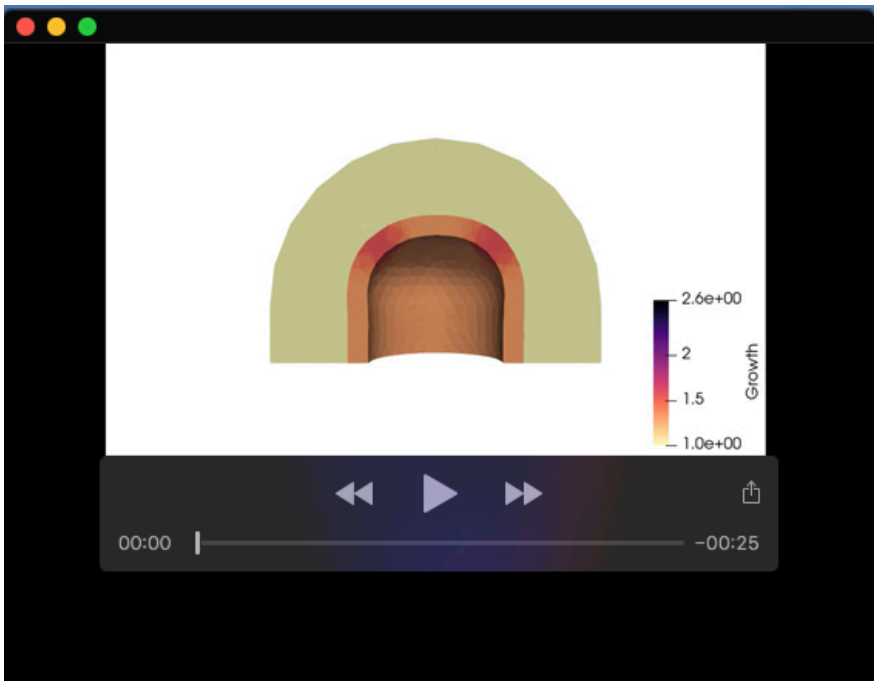

Movie 3. Computational model with increased growth along the flanks of the epithelium in a simulation with thick epithelium (t_{ep}/R_{out} = 0.12). Related to Figure 6J,K.

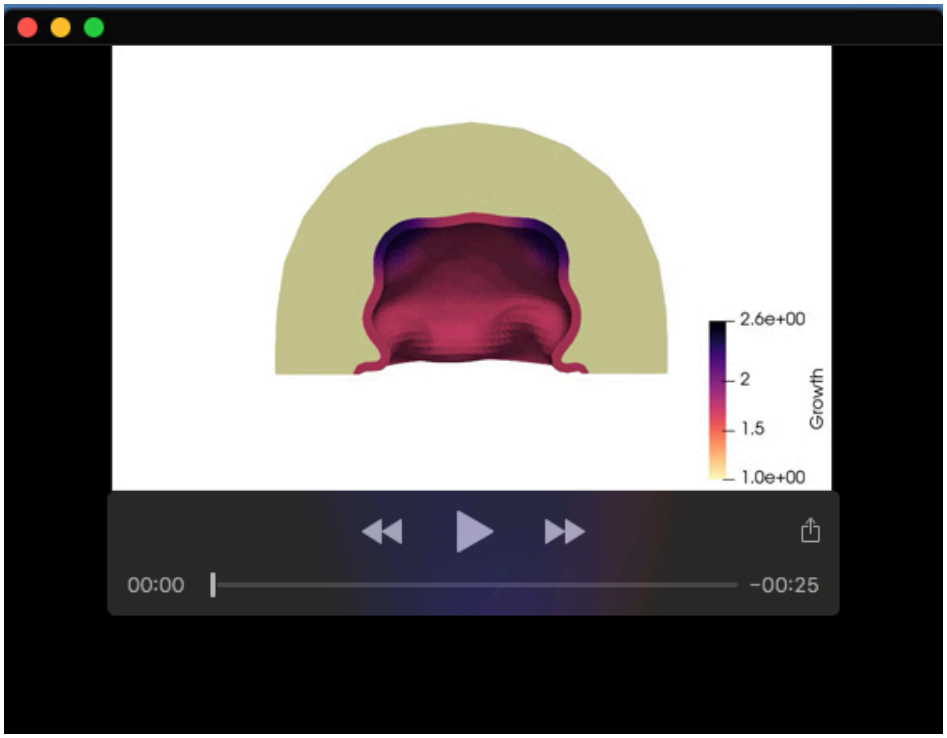

Movie 4. Computational model with increased growth along the flanks of the epithelium in a simulation with thin epithelium (t_{ep}/R_{out} = 0.05). Related to Figure 6J,L.

Supplementary Materials and Methods

Computational Model

We constructed a computational model, based on previous work (Goodwin et al., 2019; Nerger et al., 2021), of a growing epithelium surrounded by a stiff layer of smooth muscle to determine the relative roles of epithelial proliferation and smooth muscle differentiation in formation of epithelial cysts versus branches.

Geometry and physical properties

The geometry of the model consists of a short cylinder with a spherical cap on one end, comprising 3 layers around a central lumen, as shown in **Figure 6A-B**: an inner layer of epithelium surrounded by an incomplete layer of smooth muscle and an outer layer of mesenchyme, denoted as *ep*, *sm*, and *mes*, respectively. The smooth muscle wraps circumferentially around the cylindrical part of the epithelium and forms a strap around the tip of the spherical epithelial cap (**Figure 6B**).

The thicknesses of the epithelial and smooth muscle layers are denoted as t_{ep} and t_{mus}, respectively, and the overall radius of the model is denoted as R_{out}. The relative thicknesses of the layers in the model, in particular the ratio of t_{ep}/R_{out}, are based on our experimental measurements (**Figure 6B-C**).

Mechanical model

We follow (Rodriguez et al, 1994) to model tissue growth, where the shape change of tissues from the reference state is considered to be due to a combination of growth and elastic deformation. The system is assumed to be in quasi-mechanical equilibrium, since mechanical

relaxation is much faster than the processes of epithelial growth and smooth muscle differentiation. The equilibrium state can be obtained by the following energy-minimizing procedures:

Suppose that the tissue initially occupies a volume Ω in a 3D Euclidian space, with a fixed Cartesian coordinate (X_1, X_2, X_3) and an orthonormal basis $(\boldsymbol{e}_1, \boldsymbol{e}_2, \boldsymbol{e}_3)$. After some time *t*, the volume of the tissue turns into Ω_t and for each point in the reference volume, its Cartesian coordinates $\boldsymbol{X} = X_i\, \boldsymbol{e}_i$ get mapped into a difference vector $\boldsymbol{x} = x_i\, \boldsymbol{e}_i$ (summation over repeated indices is implied), and we denote such mapping as $\boldsymbol{x} = \boldsymbol{\varphi}(\boldsymbol{X})$.

Following (Ogden, 1997), shape transformation from the reference state can be described by the deformation gradient tensor $\boldsymbol{F} = \frac{\partial \boldsymbol{x}}{\partial \boldsymbol{X}}$ and, following (Rodriguez et al, 1994), we adopt the so-called multiplicative decomposition: $\boldsymbol{F} = \boldsymbol{F}^e \boldsymbol{F}^g$. This decomposition essentially assumes that the tissue first grows to an intermediate stress-free state due to $\boldsymbol{F}^g$ (often referred to as the growth tensor) and then to the final state by an additional elastic deformation due to $\boldsymbol{F}^e$. It is often more convenient to work with the displacement field $\boldsymbol{u} \equiv \boldsymbol{x} - \boldsymbol{X}$ and, hence, $\boldsymbol{F} = \boldsymbol{I} + \frac{\partial \boldsymbol{u}}{\partial \boldsymbol{X}}$ with $\boldsymbol{I}$ being the identity tensor.

We model all three layers as neo-Hookean hyperelastic solids, with the following strain energy density function (Ogden, 1997):

$$\psi\left(\boldsymbol{F}^e = \boldsymbol{F}\boldsymbol{F}^{g^{-1}}\right) = \frac{\mu}{2}(I_C^e - 3) - \mu \ln(J^e) + \frac{\lambda}{2}\ln(J^e)^2, \qquad (1)$$

where $J^e = \det(\boldsymbol{F}^e)$, $I_{\boldsymbol{C}}^e = \mathrm{trace}(\boldsymbol{C})$ and $\boldsymbol{C} = (\boldsymbol{F}^e)^T\,\boldsymbol{F}^e$ is the right Cauchy-Green tensor. λ and μ are Lamé parameters, which are related to the Young's modulus E and Poisson ratio ν through:

$$\lambda = \frac{E\nu}{(1+\nu)(1-2\nu)}, \qquad \mu = \frac{E}{2(1+\nu)}. \tag{2A,B}$$

The relative Young's moduli were estimated as reported in **Figure 6C**, and ν = 0.4 is assumed for all three layers. Gmsh was used to create a linear tetrahedral mesh for applying the finite element method (FEM) to the geometry (Geuzaine and Remacle, 2009).

Growth tensor

The growth tensor $\boldsymbol{F}^g$ uniquely determines the shape transformation due to growth. For simplicity, we assume that the undifferentiated mesenchyme and smooth muscle tissues do not grow, i.e., $\boldsymbol{F}_{mes}^g = \boldsymbol{F}_{sm}^g = \boldsymbol{I}$. Based on experimental observations, we consider the following growth tensor for the epithelium:

$$\boldsymbol{F}_{ep}^g = \boldsymbol{n} \otimes \boldsymbol{n} + g\boldsymbol{e}_{t_1} \otimes \boldsymbol{e}_{t_1} + g\boldsymbol{e}_{t_2} \otimes \boldsymbol{e}_{t_2}, \tag{3}$$

where $\boldsymbol{n}$ is the outer normal vector, and $\boldsymbol{e}_{t_1}$ and $\boldsymbol{e}_{t_2}$ are the tangent vectors of the epithelium (**Figure S7A**). At the beginning of the simulation $g = 1$. g then increases linearly for 10 timesteps until $g = 2$.

In simulations of spatially-patterned proliferation, the total growth of the epithelium g_{tot} is

$$g_{tot} = g + (g-1)\left(g_{region_1} + g_{region_2}\right) \tag{4}$$

where

$$g_{region_i} = \left(\frac{1 + \tanh\left(\frac{\phi - \frac{\phi_{pos_i} - \phi_{width}}{2}}{\theta_{trans}} \right) \tanh\left(\frac{\frac{\phi_{pos_i} + \phi_{width}}{2} - \phi}{\theta_{trans}} \right)}{2} \right) \left(\frac{1 + \tanh\left(\frac{\theta - \frac{\theta_{pos} - \theta_{height}}{2}}{\theta_{trans}} \right) \tanh\left(\frac{\frac{\theta_{pos} + \theta_{height}}{2} - \theta}{\theta_{trans}} \right)}{2} \right) \quad (5)$$

where ϕ is the azimuth angle and θ is the inclination angle and $\phi_{pos1} = 0$, $\phi_{pos2} = \pi$, $\phi_{width} = \frac{\pi}{3}$, $\theta_{pos} = \frac{\pi}{4}$, $\theta_{height} = \frac{\pi}{6}$, and $\theta_{trans} = 0.15$ (**Figure S7B-C**).

ASM differentiation

In simulations including smooth muscle, the smooth muscle wrapped around the tip of the epithelium (**Figure 6B**, red dashed box) begins the simulation with stiffness E_{mes} and increases in stiffness linearly throughout simulation time until it reaches E_{mus} at the end of the simulation. In simulations in which we modify the rate of ASM differentiation relative to epithelial proliferation, smooth muscle stiffness increases linearly but more slowly, such that at the end of simulation time the stiffness is E_{final}, where the color bar in **Figure 7C** represents $\frac{E_{final}/E_{mus}}{g_{final} - g_{initial}}$, where $g_{initial} = 1$ and $g_{final} = 2$, as defined above. The smooth muscle around the flanks of the epithelium (**Figure 6A**, magenta) has modulus E_{mus} throughout all simulations.

Boundary conditions

The bottom surface of the model $\partial\Omega_b$ has a fixed displacement $u_3 = 0$. The displacement of the point at the distal tip of the top of the mesenchyme has a fixed displacement of $u_1 = u_2 = 0$ to prevent translation of the structure, and a point on $\partial\Omega_b$ on the outer circumference of the mesenchyme has a fixed displacement of $u_2 = 0$ to prevent rotation of the structure.

The outside surface of the mesenchyme is considered traction-free, but the inner surface of the epithelium, $\partial\Omega^{in}$, has a positive pressure opposite to the normal vector $\boldsymbol{n}$ at every point such that the traction force $\boldsymbol{t}$:

$$\boldsymbol{t} = -p\boldsymbol{n}, \tag{6}$$

where $p = 0.1E_{mes}$ (Chevalier et al., 2016; Nelson et al., 2017). And $\boldsymbol{n}$ is the outer normal vector of $\partial\Omega^{in}$ in the deformed state.

Finite element method

The equilibrium state of the system at each time step can be determined by obtaining the stationary point of the following potential energy function (Dervaux and Ben Amar, 2011):

$$\Pi = \int_{\Omega} J^{g}\psi(\boldsymbol{F}^{e})\ dX - \int_{\Omega} \boldsymbol{B}\cdot\boldsymbol{u}\, dX - \int_{\partial\Omega_{t}^{in}} \boldsymbol{t}\cdot\boldsymbol{u}\, ds, \tag{7}$$

where Ω is the whole domain of the reference state, dX is an infinitesimal volume element of the domain, $\boldsymbol{B} = 0$ everywhere on Ω because no body-force is applied to the structure, $\partial\Omega_{t}^{in}$ represents the luminal boundary of the epithelium in the deformed configuration, and ds is an infinitesimal element of the boundary in the deformed state. The stationary point of the above potential energy can be obtained by solving the following equation:

$$0 = \delta\Pi = \delta\int_{\Omega} J^{g}\psi(\boldsymbol{F}^{e})\ dX + \int_{\partial\Omega^{in}} p\,\boldsymbol{n}\cdot\delta\boldsymbol{u}\, dS \tag{8A}$$

$$= \delta\int_{\Omega} J^{g}\psi(\boldsymbol{F}^{e})\ dX + \int_{\partial\Omega^{in}} p(J\boldsymbol{F}^{-T}\boldsymbol{N})\cdot\delta\boldsymbol{u}\, dS \tag{8B}$$

where $\partial\Omega^{in}$ and dS are the luminal boundary and the infinitesimal surface elements of the luminal boundary of the undeformed epithelial domain, respectively.

We used the FEM to solve the above minimization problem numerically (Bathe, 1996). Using the tetrahedral mesh generated by Gmsh to discretize the domain Ω, we solved for $\boldsymbol{u}$ at each timestep using the open-source FEniCS software (Logg et al., 2012) to apply the Newton-Raphson algorithm (Atkinson, 1989) in each element of the mesh. Where the Newton-Raphson algorithm failed to converge, we applied the dynamic relaxation method (Underwood, 1983) to find the $\boldsymbol{u}$ that minimized the problem. The results were visualized in the open-source tool Paraview (Squillacote and Ahrens, 2006).

The solution was tested to be robust to mesh refinements. The basic physics of the simulation was tested by inspecting the results of simulations with pressure in the lumen but without epithelial growth to ensure the model expanded in this case as expected.

Supplementary References

Atkinson, K. E. (1989). *An introduction to numerical analysis* (2nd edn). New York: Wiley.

Bathe, K.-J. (1996). *Finite element procedures*. Englewood Cliffs, N.J.: Prentice Hall.

Chevalier, N. R., Gazquez, E., Dufour, S. and Fleury, V. (2016). Measuring the micromechanical properties of embryonic tissues. *Methods* **94**, 120-128.

Dervaux, J. and Ben Amar, M. (2011). Buckling condensation in constrained growth. *J. Mech. Phys. Solids* **59**, 538-560.

Geuzaine, C. and Remacle, J. F. (2009). Gmsh: A 3-D finite element mesh generator with built-in pre- and post-processing facilities. *Int. J. Numer. Meth. Eng.* **79**, 1309-1331.

Goodwin, K., Mao, S., Guyomar, T., Miller, E., Radisky, D. C., Kosmrlj, A. and Nelson, C. M. (2019). Smooth muscle differentiation shapes domain branches during mouse lung development. *Development* **146**, 1-13.

Hayashi, K., Nakamura, S., Nishida, W. and Sobue, K. (2006). Bone morphogenetic protein-induced MSX1 and MSX2 inhibit myocardin-dependent smooth muscle gene transcription. *Mol Cell Biol* **26**, 9456-9470.

Lee, K., Chen, Q. K., Lui, C., Cichon, M. A., Radisky, D. C. and Nelson, C. M. (2012). Matrix compliance regulates Rac1b localization, NADPH oxidase assembly, and epithelial-mesenchymal transition. *Mol. Biol. Cell* **23**, 4097-4108.

Logg, A., Mardal, K.-A. and Wells, G. (2012). *Automated Solution of Differential Equations by the Finite Element Method : The FEniCS Book*. Heidelberg: Springer.

Nelson, C. M., Gleghorn, J. P., Pang, M. F., Jaslove, J. M., Goodwin, K., Varner, V. D., Miller, E., Radisky, D. C. and Stone, H. A. (2017). Microfluidic chest cavities reveal that transmural pressure controls the rate of lung development. *Development* **144**, 4328-4335.

Nerger, B. A., Jaslove, J. M., Elashal, H. E., Mao, S., Kosmrlj, A., Link, A. J. and Nelson, C. M. (2021). Local accumulation of extracellular matrix regulates global morphogenetic patterning in the developing mammary gland. *Curr. Biol.*, 1-15.

Ng-Blichfeldt, J. P., Schrik, A., Kortekaas, R. K., Noordhoek, J. A., Heijink, I. H., Hiemstra, P. S., Stolk, J., Konigshoff, M. and Gosens, R. (2018). Retinoic acid signaling balances adult distal lung epithelial progenitor cell growth and differentiation. *EBioMedicine* **36**, 461-474.

Ogden, R. W. (1997). *Non-linear elastic deformations*. Mineola, N.Y.: Dover Publications.

Schlesinger, J., Schueler, M., Grunert, M., Fischer, J. J., Zhang, Q., Krueger, T., Lange, M., Tonjes, M., Dunkel, I. and Sperling, S. R. (2011). The cardiac transcription

network modulated by Gata4, Mef2a, Nkx2.5, Srf, histone modifications, and microRNAs. *PLoS Genet.* **7**, e1001313; 1001311-1001316.

Sousa, A. M., Liu, T., Guevara, O., Stevens, J., Fanburg, B. L., Gaestel, M., Toksoz, D. and Kayyali, U. S. (2007). Smooth muscle alpha-actin expression and myofibroblast differentiation by TGFbeta are dependent upon MK2. *J. Cell. Biochem.* **100**, 1581-1592.

Squillacote, A. H. and Ahrens, J. (2006). *The ParaView guide*. Clifton Park, NY: Kitware.

Tanaka, T., Sato, H., Doi, H., Yoshida, C. A., Shimizu, T., Matsui, H., Yamazaki, M., Akiyama, H., Kawai-Kowase, K., Iso, T., et al. (2008). Runx2 represses myocardin-mediated differentiation and facilitates osteogenic conversion of vascular smooth muscle cells. *Mol Cell Biol* **28**, 1147-1160.

Underwood, P. (1983). Dynamic Relaxation. In *Computational methods for Transient Analysis* (ed. T. Belytschko & T. J. R. Hughes), pp. 245-265. Amsterdam Netherlands: North-Holland Pub.

Visel, A., Thaller, C. and Eichele, G. (2004). GenePaint.org: an atlas of gene expression patterns in the mouse embryo. *Nucleic Acids Res.* **32**, D552-556.

Wilczewski, C. M., Hepperla, A. J., Shimbo, T., Wasson, L., Robbe, Z. L., Davis, I. J., Wade, P. A. and Conlon, F. L. (2018). CHD4 and the NuRD complex directly control cardiac sarcomere formation. *Proc. Natl. Acad. Sci. U. S. A.* **115**, 6727-6732.